PCCP

ROYAL SOCIETY OF CHEMISTRY

PAPER

View Article Online
View Journal | View Issue



Cite this: *Phys. Chem. Chem. Phys.*, 2024, **26**, 14613

# Mechanism of $CO_2$ in promoting the hydrogenation of levulinic acid to γ-valerolactone catalyzed by $RuCl_3$ in aqueous solution†

Han-Yun Min, [a] Jin-Shan Xiong, [a] Ting-Hao Liu, [a] Shuai Fu, [a] Chang-Wei Hu [b] and Hua-Qing Yang *[a]

A Ru-containing complex shows good catalytic performance toward the hydrogenation of levulinic acid (LA) to γ-valerolactone (GVL) with the assistance of organic base ligands (OBLs) and $CO_2$. Herein, we report the competitive mechanisms for the hydrogenation of LA to GVL, 4-oxopentanal (OT), and 2-methyltetrahydro-2,5-furandiol (MFD) with HCOOH or $H_2$ as the H source catalyzed by $RuCl_3$ in aqueous solution at the M06/def2-TZVP, 6-311++G(d,p) theoretical level. Kinetically, the hydrodehydration of LA to GVL is predominant, with OT and MFD as side products. With HCOOH as the H source, initially, the OBL (triethylamine, pyridine, or triphenylphosphine) is responsible for capturing $H^+$ from HCOOH, leading to $HCOO^-$ and $[HL]^+$. Next, the $Ru^{3+}$ site is in charge of sieving $H^-$ from $HCOO^-$, yielding $[RuH]^{2+}$ hydride and $CO_2$. Alternatively, with $H_2$ as the H source, the OBL stimulates the heterolysis of H–H bond with the aid of $Ru^{3+}$ active species, producing $[RuH]^{2+}$ and $[HL]^+$. Toward the $[RuH]^{2+}$ formation, $H_2$ as the H source exhibits higher activity than HCOOH as the H source in the presence of an OBL. Thereafter, $H^-$ in $[RuH]^{2+}$ gets transferred to the unsaturated C site of ketone carbonyl in LA. Afterwards, the $Ru^{3+}$ active species is capable of cleaving the C–OH bond in 4-hydroxyvaleric acid, yielding $[RuOH]^{2+}$ hydroxide and GVL. Subsequently, $CO_2$ promotes Ru–OH bond cleavage in $[RuOH]^{2+}$, forming $HCO_3^-$ and regenerating the $Ru^{3+}$-active species owing to its Lewis acidity. Lastly, between the resultant $HCO_3^-$ and $[HL]^+$, a neutralization reaction occurs, generating $H_2O$, $CO_2$, and OBLs. Thus, the present study provides insights into the promotive roles of additives such as $CO_2$ and OBLs in Ru-catalyzed hydrogenation.

Received 21st February 2024,
Accepted 27th April 2024

DOI: 10.1039/d4cp00753k

rsc.li/pccp



## 1. Introduction

Currently, with the rapid consumption of fossil resources, tremendous efforts are directed towards converting renewable biomass into fuels and value-added chemicals.[1] Carbohydrates, one of the major components of plant biomass, can be selectively dehydrated into levulinic acid (LA), which is a very attractive C5 platform chemical because of its characteristic carboxyl (–COOH) and carbonyl (–C=O) groups.[2] In particular, the hydrogenation of LA to γ-valerolactone (GVL) has become increasingly attractive[3–6] since GVL can be widely used as a highly effective fuel additive, food additive, green solvent, and intermediate for biobased polymers.[7–9]

To date, both heterogeneous and homogeneous catalysts have been widely used in the selective hydrogenation of LA to GVL. Heterogeneous catalysts, *i.e.*, Ru-,[9–14] Pt-,[15] Fe-,[16] Co-,[17] Ni-,[18] and Cu-based catalysts,[16,19] exhibit good activity for LA hydrogenation. Compared with heterogeneous catalysts, homogeneous catalysts, including Ru-,[20–24] Ir-,[25–27] Pt-,[28] and Ni-containing complexes,[5,29] have higher catalytic efficiency and selectivity under mild reaction conditions. Noteworthily, Ru-containing complexes show excellent catalytic performance. Interestingly, Fu's group has pioneeringly conducted research on the hydrogenation of LA to GVL catalyzed by $RuCl_3{\cdot}3H_2O$ with organic base ligands using HCOOH or $H_2$ as the hydrogen (H) source in aqueous solution.[20] With $H_2$ as the H source, $CO_2$ addition can greatly improve Ru-catalyzed hydrogenation; however, $CO_2$ acts as a decomposition product with HCOOH as the H source.[20] Notably, supercritical $CO_2$ is also used as a medium for LA-to-GVL hydrogenation in heterogeneous catalytic systems.[30] However, this striking positive effect of $CO_2$ on

[a] College of Chemical Engineering, Sichuan University, Chengdu, Sichuan, 610065, P. R. China. E-mail: huaqingyang@scu.edu.cn; Fax: +86 28 85464466; Tel: +86 28 85464466

[b] Key Laboratory of Green Chemistry and Technology, Ministry of Education, College of Chemistry, Sichuan University, Chengdu, Sichuan, 610064, P. R. China

† Electronic supplementary information (ESI) available: Geometric structures, data of energies, relative Gibbs free energies. The geometric structures of various species. See DOI: https://doi.org/10.1039/d4cp00753k

Ru-catalyzed hydrogenation at the molecular level remains unclear.

In this work, we aim to theoretically explore the molecular mechanism underlying the hydrogenation of LA to GVL catalyzed by $RuCl_3$ with an organic base ligand in aqueous solution using HCOOH or $H_2$ as the H source. The objectives are as follows: (a) to ascertain the catalytically active species of $RuCl_3 \cdot 3H_2O$ in aqueous solution, (b) to clarify the difference in the reduction mechanism between HCOOH and $H_2$ as the H source, (c) to elucidate the role of organic base ligands, and (d) to understand the origin of the promotive effect of $CO_2$ in Ru-catalyzed hydrogenation.

## 2. Computational methods

In an aqueous solution, all geometric calculations were performed using the program Gaussian 09.[31] A polarizable continuum model based on solute electron density (PCM-SMD) was applied to simulate the solvent effect of the aqueous solution.[32,33] Full geometry optimizations were carried out to locate all the stationary points and transition states *via* a hybrid M06 functional method[34] with the def2-TZVP basis set[35] and the corresponding effective core potential (ECP) for the Ru element; the 6-311++G(d,p) basis set[36,37] for C, H, O, N, and P elements in the reaction region; and the 6-31G(d,p) basis set[38] for C and H elements of the phenyl group, namely M06/def2-TZVP, 6-311++G(d,p).

Harmonic frequency calculations were employed to verify the stationary points and obtain corrections of the zero-point energy (ZPE) as well as the thermal correction of the Gibbs free energy ($G_0$). For reaction pathway analysis, each transition structure was verified to have only one imaginary frequency, and the connections between transition states and corresponding intermediates were verified through intrinsic reaction coordinate (IRC) calculations.[39,40] The natural charges were gained using natural bond orbital (NBO) analysis.[41,42] The differential electron localization function of species was analyzed by using the Multiwfn package.[43,44] Unless otherwise specified, the Gibbs free energy of formation ($\Delta G$) is relative to the initial catalytically active species and reactants obtained at the M06/6-311++G(d,p), def2-TZVP level in the aqueous solution under experimental temperature and pressure (423 K and 80 atm).[20]

The rate constants were assessed over the 403–443 K temperature range, on the basis of conventional transition state theory, together with tunneling correction, as described in our previous study.[45,46]

## 3. Results and discussion

In LA, there are two kinds of carbonyl groups, *i.e.*, ketone carbonyl and carboxyl carbonyl. Then, the hydrogenations of these carbonyl groups are competitive with each other. For the hydrogenation of LA with HCOOH or $H_2$ as the H source, the possible reaction pathways are depicted in Scheme 1.

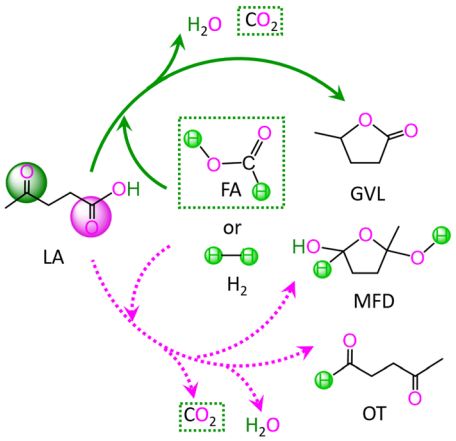


Scheme 1 Reaction pathway for the conversion of levulinic acid (LA) to γ-valerolactone (GVL), 2-methyltetrahydro-2,5-furandiol (MFD) and 4-oxopentanal (OT) with HCOOH and $H_2$ as the H source.

As depicted in Scheme 1, with HCOOH as the H source, reaction (I) is associated with the hydrodehydration of LA to GVL through ketone carbonyl, reaction (II) is concerned with the hydrodehydration of LA to 4-oxopentanal (OT) through carboxyl carbonyl, and reaction (III) is related to the hydrogenation of LA to 2-methyltetrahydro-2,5-furandiol (MFD) through carboxyl carbonyl. Alternatively, with $H_2$ as the H source, reaction IV denotes the hydrodehydration of LA to GVL through ketone carbonyl, reaction V signifies the hydrodehydration of LA to OT through carboxyl carbonyl, and reaction VI expresses the hydrogenation of LA to MFD through carboxyl carbonyl. These six gross reactions (I)–(VI) are listed as follows:

$$LA + HCOOH \rightarrow GVL + H_2O + CO_2 \quad (I)$$

$$LA + HCOOH \rightarrow OT + H_2O + CO_2 \quad (II)$$

$$LA + HCOOH \rightarrow MFD + CO_2 \quad (III)$$

$$LA + H_2 \rightarrow GVL + H_2O \quad (IV)$$

$$LA + H_2 \rightarrow OT + H_2O \quad (V)$$

$$LA + H_2 \rightarrow MFD \quad (VI)$$

### 3.1 Ru-containing active species of $RuCl_3 \cdot 3H_2O$ in aqueous solution

In aqueous solution, $RuCl_3 \cdot 3H_2O$ should dissociate into $Ru^{3+}$ cation and $Cl^-$ anion. Here, the ground state of $Ru^{3+}$ cation is the sextet state, with the quartet state and doublet state as the excited states, which locate 214.5 and 421.8 kJ $mol^{-1}$ above the ground sextet state, respectively, as shown in Fig. S1 from the ESI.† The superscript prefixes "$^2$", "$^4$", and "$^6$" represent the doublet, quartet, and sextet states, respectively. Unless specified, the default state is the singlet ground state "$^1$". Based on the experimental literature in aqueous solution,[20] additives are associated with organic base ligands (OBLs), *i.e.*, triphenylphosphine ($PPh_3$), triethylamine ($NEt_3$), and

 

pyridine (PY). After that, $H_2O$, $PPh_3$, $NEt_3$, and PY may coordinate to the $Ru^{3+}$-center. Thereupon, we will discuss the stabilities of coordinated Ru-containing species in aqueous solution thermodynamically.

As shown in Fig. S1 from ESI,† initially, the coordination of $H_2O$ to the $^6Ru^{3+}$-center is calculated to be thermodynamically unfavorable. That is to say, when $RuCl_3{\cdot}3H_2O$ dissolves in aqueous solution, $Ru^{3+}$ cation does not coordinate with solvent water molecules. Considering the coordination of the ligand to $^6Ru^{3+}$-center in aqueous solution, the values of $G_r$ are −16.1, 8.2, 12.1, and 22.0 kJ mol$^{-1}$, for $^6[Ru(PPh_3)]^{3+}$, $^6[Ru(NEt_3)]^{3+}$, $^6[Ru(H_2O)]^{3+}$, and $^6[Ru(PY)]^{3+}$ complexes, respectively, as shown in Fig. S2 from ESI.† Among the four ligands of $PPh_3$, $NEt_3$, $H_2O$, and PY, only $PPh_3$ can coordinate to the $^6Ru^{3+}$-center, forming a stable complex $^6[Ru(PPh_3)]^{3+}$. Thereupon, $^6[Ru(PPh_3)]^{3+}$ is preferred as the initial catalytically active species.

### 3.2 Reaction I: LA + HCOOH → GVL + $H_2O$ + $CO_2$

With HCOOH as the hydrogen source, the hydrodehydration of LA to GVL includes the following five reaction stages, *i.e.*,

$$HCOOH + L \rightarrow HCOO^- + [HL]^+ \text{ (L = } PPh_3, NEt_3, \text{ and PY)} \quad \text{(i)}$$

$$HCOO^- + {}^6[Ru(PPh_3)]^{3+} \rightarrow {}^6[RuH]^{2+} + PPh_3 + CO_2 \quad \text{(ii)}$$

$$^6[RuH]^{2+} + LA \rightarrow {}^6[RuOH]^{2+} + GVL \quad \text{(iii)}$$

$$^6[RuOH]^{2+} + CO_2 + PPh_3 \rightarrow {}^6[Ru(PPh_3)]^{3+} + HCO_3^- \quad \text{(iv)}$$

$$HCO_3^- + [HL]^+ \rightarrow L + CO_2 + H_2O \text{ (L = } PPh_3, NEt_3, \text{ and PY)} \quad \text{(v)}$$

**3.2.1 Reaction stage (i): HCOOH + L → $HCOO^-$ + $[HL]^+$ (L = $PPh_3$, $NEt_3$, and PY).** Reaction stage (i) is concerned with the proton–exchange between HCOOH and organic base ligand (OBL, L = $PPh_3$, $NEt_3$, and PY), producing $HCOO^-$ anion and $[HL]^+$ cation. The geometric structures and potential energy diagrams for the reaction stage (i) of HCOOH + L → $HCOO^-$ + $[HL]^+$ (L = $PPh_3$, $NEt_3$, and PY) are depicted in Fig. 1, marked as **1-F-P**, **1-F-N**, and **1-F-Y**, respectively.

As shown in Fig. 1, the $\Delta G$s of reaction stage (i) of HCOOH + L → $HCOO^-$ + $[HL]^+$ (L = $PPh_3$, $NEt_3$, and PY) are 3.2, −26.6, and 2.6 kJ mol$^{-1}$, respectively, while $\Delta E$s are calculated to be 1.0, −28.5, and 1.8 kJ mol$^{-1}$. It is inferred that the $NEt_3$ ligand is thermodynamically favourable, whereas both $PPh_3$ and PY are thermodynamically unfavourable, grabbing the proton $H^+$ from HCOOH. On the other hand, kinetically, reaction stage (i) comprises three typical reaction steps, *i.e.*, (1) the formation of a molecular complex between HCOOH and ligand, (2) the proton-exchange *via* a three-membered linear transition state (TS), and (3) the dissociation of the resultant products ($HCOO^-$ + $[HL]^+$). The **1-F-P** includes an energy height of the highest point (EHHP) of 47.1 kJ mol$^{-1}$ at 1-F-P-TS1 and the highest energy requirement (HER) of 25.3 kJ mol$^{-1}$ at the reaction step of (HCOOH + $PPh_3$) → 1-F-P-IM1. The **1-F-N** involves the EHHP of 42.4 kJ mol$^{-1}$ at **1-F-N**-TS1 and the HER of 41.7 kJ mol$^{-1}$ at the reaction step of (HCOOH + $NEt_3$) → 1-F-N-IM1. The **1-F-Y** contains the EHHP of 13.5 kJ mol$^{-1}$ at **1-F-Y**-TS1 and the HER of 10.9 kJ mol$^{-1}$ at the reaction step of (HCOOH + PY) → 1-F-Y-IM1. It is indicated that these ligands kinetically increase as $PPh_3$ < $NEt_3$ < PY in capturing the proton $H^+$ from HCOOH, because of their corresponding EHHP of 47.1, 42.4, and 13.5 kJ mol$^{-1}$. One can conclude that $NEt_3$ ligand should be preferable in grabbing the proton $H^+$ from HCOOH both thermodynamically and kinetically. This result is in good agreement with the experimental observation, in which the additive $NEt_3$ plays an excellently promotive role in the Ru-catalyzed hydrogenation of LA to GVL.[20]

**3.2.2 Reaction stage (ii): $HCOO^-$ + $^6[Ru(PPh_3)]^{3+}$ → $^6[RuH]^{2+}$ + $PPh_3$ + $CO_2$.** Reaction stage (ii) is associated with the ligand–exchange between the $^6[Ru(PPh_3)]^{3+}$ complex and $HCOO^-$ anion, and then $^6Ru^{3+}$ cation capturing $H^-$ anion from $HCOO^-$, forming $^6[RuH]^{2+}$ hydride with the release of $CO_2$. The geometric structures and potential energy diagrams for the reaction stage (ii) of $HCOO^-$ + $^6[Ru(PPh_3)]^{3+}$ → $^6[RuH]^{2+}$ + $PPh_3$ + $CO_2$ are displayed in Fig. 2, marked as **2-F-S.**

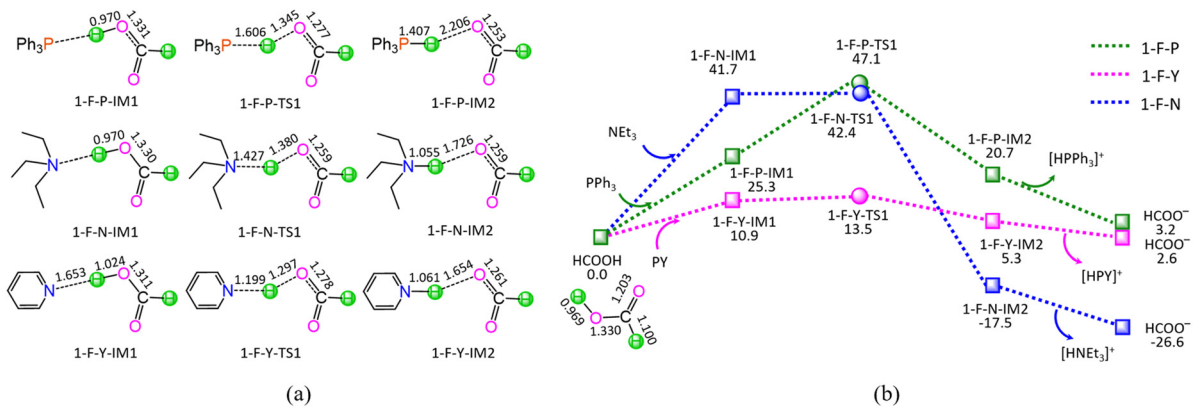


Fig. 1 The optimized geometric structures (a) and schematic energy diagrams (b) with the relative Gibbs free energies ($G_r$, kJ mol$^{-1}$) for the proton–exchange reaction stage (i) of HCOOH + L → $HCOO^-$ + $[HL]^+$ (L = $PPh_3$, $NEt_3$, and PY).

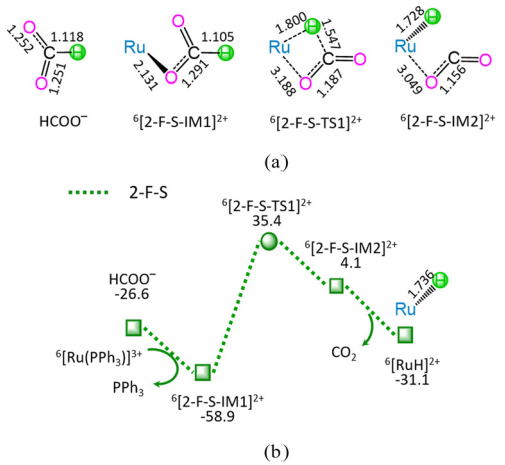


Fig. 2 The geometric structures (a) and schematic energy diagrams (b) with the relative Gibbs free energy ($G_r$, kJ mol$^{-1}$) for the reaction stage (ii) of $HCOO^-$ + $^6[Ru(PPh_3)]^{3+}$ → $^6[RuH]^{2+}$ + $PPh_3$ + $CO_2$. For clarity, hydrogen atoms on carbon are omitted. Bond lengths are presented in Å.

As shown in Fig. 2, the reaction stage (ii) of $HCOO^-$ + $^6[Ru(PPh_3)]^{3+}$ → $^6[RuH]^{2+}$ + $PPh_3$ + $CO_2$ comprises three typical reaction steps, *i.e.*, (1) the ligand–exchange between the $^6[Ru(PPh_3)]^{3+}$ complex and $HCOO^-$ anion, forming a $^6[2\text{-F-S-IM1}]^{2+}$ complex, (2) both C–H bond cleavage and Ru–H bond formation *via* a four-membered cyclic $^6[2\text{-F-S-TS1}]^{2+}$ through a [1,3]-H-shift, yielding a molecular complex $^6[2\text{-F-S-IM2}]^{2+}$, and (3) the dissociation of $^6[2\text{-F-S-IM2}]^{2+}$, producing both $^6[RuH]^{2+}$ hydride and free $CO_2$. The **2-F-S** involves the EHHP of 35.4 kJ mol$^{-1}$ at $^6[2\text{-F-S-TS1}]^{2+}$ and HER of 94.3 kJ mol$^{-1}$ at the reaction step of $^6[2\text{-F-S-IM1}]^{2+}$ → $^6[2\text{-F-S-TS1}]^{2+}$ → $^6[2\text{-F-S-IM2}]^{2+}$.

**3.2.3 Reaction stage (iii): $^6[RuH]^{2+}$ + LA → $^6[RuOH]^{2+}$ + GVL.** Reaction stage (iii) is related to the hydrogenation of LA with $^6[RuH]^{2+}$ hydride, yielding GVL and $^6[RuOH]^{2+}$ hydroxide. The geometric structures and potential energy diagrams for the reaction stage (iii) of $^6[RuH]^{2+}$ + LA → $^6[RuOH]^{2+}$ + GVL are depicted in Fig. 3, through the initial interaction of Ru site with ketone carbonyl and carboxyl carbonyl of LA, marked as **3-F-K** and **3-F-C**, respectively.

As shown in Fig. 3, the **3-F-K** comprises seven successive reaction steps, *i.e.*, (1) the formation of a molecular complex $^6[3\text{-F-K-IM4}]^{2+}$ through the initial interaction of Ru-site with ketone carbonyl of LA, (2) a [2 + 2] addition at ketone carbonyl *via* four-membered cyclic $^6[3\text{-F-K-TS2}]^{2+}$ through a [1,3]-H shift with Ru–H bond cleavage, (3) the molecular rearrangement between $^6[3\text{-F-K-IM5}]^{2+}$ and $^6[3\text{-F-K-IM6}]^{2+}$, (4) the ring-closure with C1–O bond formation *via* a seven-membered envelope $^6[3\text{-F-K-TS3}]^{2+}$, (5) the molecular rearrangement between $^6[3\text{-F-K-IM7}]^{2+}$ and $^6[3\text{-F-K-IM8}]^{2+}$, (6) the formation of GVL with both C1–OH bond cleavage and Ru–OH bond formation through four-membered cyclic $^6[3\text{-F-K-TS4}]^{2+}$, and (7) the release of GVL from $^6[3\text{-F-K-IM9}]^{2+}$, leaving $^6[RuOH]^{2+}$ hydroxide behind. The **3-F-K** includes the EHHP of 56.3 kJ mol$^{-1}$ at $^6[3\text{-F-K-TS2}]^{2+}$ and HER of 76.1 kJ mol$^{-1}$ at the reaction step of $^6[3\text{-F-K-IM6}]^{2+}$ → $^6[3\text{-F-K-TS3}]^{2+}$ → $^6[3\text{-F-K-IM7}]^{2+}$ for the ring-closure with C1–O bond formation.

Additionally, between **3-F-C** and **3-F-K**, the reaction pathway differs from ($^6[RuH]^{2+}$ + LA) to $^6[3\text{-F-K-IM6}]^{2+}$, whereas the remaining reaction pathways from $^6[3\text{-F-K-IM6}]^{2+}$ to ($^6[RuOH]^{2+}$ + GVL) are identical to each other. The **3-F-C** from ($^6[RuH]^{2+}$ + LA) to $^6[3\text{-F-K-IM6}]^{2+}$ involves two reaction steps, *i.e.*, (1) the formation of a molecular complex $^6[3\text{-F-C-IM4}]^{2+}$ through the initial interaction of Ru-site with the carboxyl carbonyl of LA, and (2) a [2 + 5] addition at ketone carbonyl *via* seven-membered cyclic $^6[3\text{-F-C-TS2}]^{2+}$ through a [1,6]-H shift with Ru–H bond cleavage. The **3-F-C** possesses the EHHP of 68.6 kJ mol$^{-1}$ at $^6[3\text{-F-C-TS2}]^{2+}$ and HER of 76.1 kJ mol$^{-1}$ at the reaction step of $^6[3\text{-F-K-IM6}]^{2+}$ → $^6[3\text{-F-K-TS3}]^{2+}$ → $^6[3\text{-F-K-IM7}]^{2+}$ for the ring-closure with C1–O bond formation.

Compared with **3-F-C**, **3-F-K** is kinetically more favorable, owing to its lower EHHP (56.3 *vs.* 68.6 kJ mol$^{-1}$). That is to say, for reaction stage (iii), the optimal reaction pathway kinetically proceeds through the initial interaction of Ru-site with ketone carbonyl rather than carboxyl carbonyl.

**3.2.4 Reaction stage (iv): $^6[RuOH]^{2+}$ + $CO_2$ + $PPh_3$ → $^6[Ru(PPh_3)]^{3+}$ + $HCO_3^-$.** Reaction stage (iv) is associated with the neutralization reaction between $^6[RuOH]^{2+}$ hydroxide and $CO_2$ Lewis acid, producing $HCO_3^-$ and regenerating catalytically active species $^6[Ru(PPh_3)]^{3+}$. The geometric structures and potential energy diagrams for the reaction stage (iv) of $^6[RuOH]^{2+}$ + $CO_2$ + $PPh_3$ → $^6[Ru(PPh_3)]^{3+}$ + $HCO_3^-$ are displayed in Fig. 4, marked as **4-F-C**.

As depicted in Fig. 4, in the absence of $CO_2$ (marked as **4-F-N**), the ligand–exchange between $^6[RuOH]^{2+}$ and $PPh_3$ requires the energy of 128.4 kJ mol$^{-1}$, producing $^6[Ru(PPh_3)]^{3+}$ and $OH^-$ anion. Alternatively, the **4-F-C** comprises three successive reaction steps, *i.e.*, (1) the formation of a molecular complex $^6[4\text{-F-C-IM11}]^{2+}$, (2) both Ru–OH bond cleavage and C–OH bond formation *via* four-membered cyclic $^6[4\text{-F-C-TS5}]^{2+}$, and (3) the ligand–exchange between $^6[4\text{-F-C-IM12}]^{2+}$ and $PPh_3$, yielding $HCO_3^-$ and regenerating catalytically active species $^6[Ru(PPh_3)]^{3+}$. The **4-F-C** contains the EHHP of −33.3 kJ mol$^{-1}$ at $^6[4\text{-F-C-TS5}]^{2+}$ and the HER of 45.0 kJ mol$^{-1}$ at the reaction step of $^6[4\text{-F-C-IM11}]^{2+}$ → $^6[4\text{-F-C-TS5}]^{2+}$ → $^6[4\text{-F-C-IM12}]^{2+}$ for the Ru–OH bond cleavage and C–OH bond formation.

Compared with **4-F-N**, **4-F-C** is kinetically more preferable, thanks to its lower EHHP (−33.3 *vs.* 15.3 kJ mol$^{-1}$) and its lower HER (45.0 *vs.* 128.4 kJ mol$^{-1}$). This embodies that $CO_2$ facilitates the Ru–OH bond cleavage in $[RuOH]^{2+}$ hydroxide, owing to its Lewis-acidity.

**3.2.5 Reaction stage (v): $HCO_3^-$ + $[HL]^+$ → L + $CO_2$ + $H_2O$ (L = $PPh_3$, $NEt_3$, and PY).** Reaction stage (v) is associated with the neutralization reaction between $HCO_3^-$ Brønsted base and $[HL]^+$ Brønsted acid, with the reduction of ligand (L = $PPh_3$, $NEt_3$, and PY) and the release of $CO_2$. The geometric structures and potential energy diagrams for the reaction stage (v) of $HCO_3^-$ + $[HL]^+$ → L + $CO_2$ + $H_2O$ (L = $PPh_3$, $NEt_3$, and PY) are depicted in Fig. 5, marked as **5-B-P**, **5-B-N**, and **5-B-Y**, respectively.

As shown in Fig. 5, the $\Delta G$ of reaction stage (v) of $HCO_3^-$ + $[HL]^+$ → L + $CO_2$ + $H_2O$ (L = $PPh_3$, $NEt_3$, and PY) is −53.1, −23.3, and −52.5 kJ mol$^{-1}$, respectively. It is indicated that the neutralization reaction of reaction stage (v) is thermodynamically favorable. Alternatively, reaction stage (v) is composed of three

 

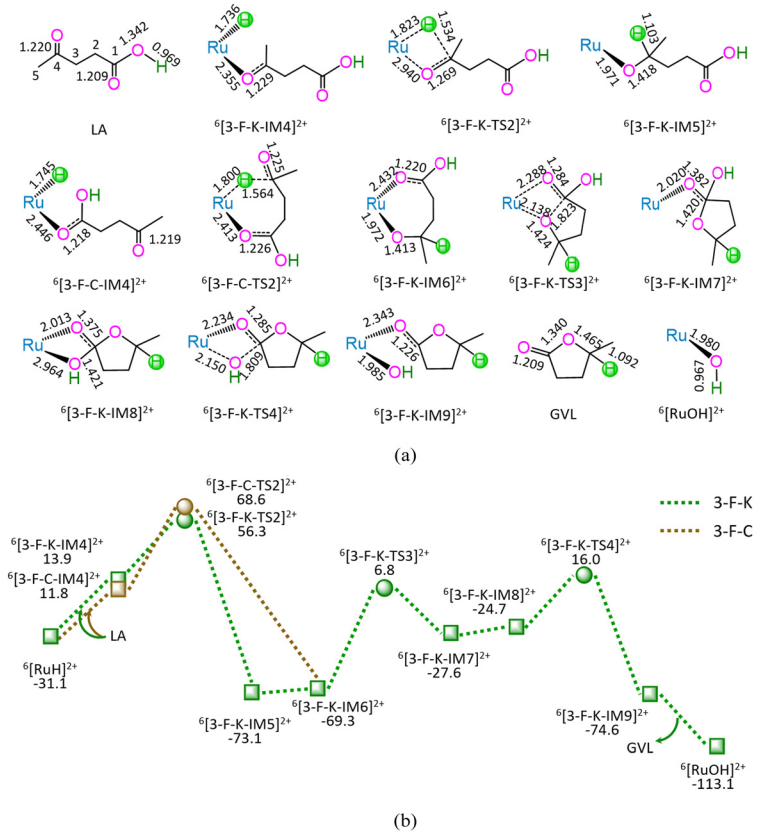


Fig. 3 The geometric structures (a) and the schematic energy diagrams (b) with the relative Gibbs free energy ($G_r$, kJ mol$^{-1}$) for the reaction stage (iii) of $^6$[RuH]$^{2+}$ + LA → $^6$[RuOH]$^{2+}$ + GVL through the hydrogenation of ketone carbonyl. For clarity, hydrogen atoms on carbon are omitted. Bond lengths are presented in Å.

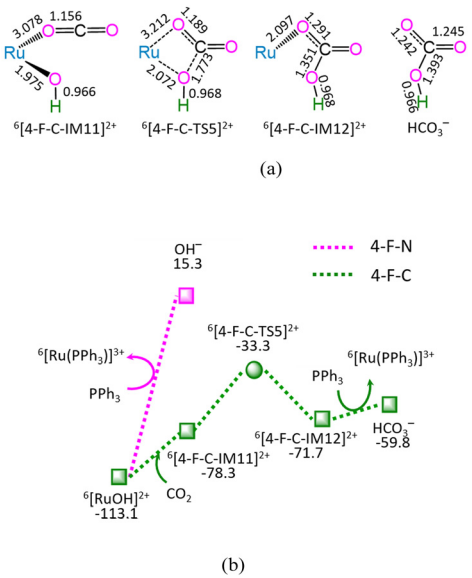


Fig. 4 The geometric structures (a) and the schematic energy diagrams (b) with the relative Gibbs free energy ($G_r$, kJ mol$^{-1}$) for the reaction stage (iv) of $^6$[RuOH]$^{2+}$ + $CO_2$ + $PPh_3$ → $^6$[Ru(PPh$_3$)]$^{3+}$ + $HCO_3^-$. For clarity, hydrogen atoms on carbon are omitted. Bond lengths are presented in Å.

typical reaction steps, *i.e.*, (1) the formation of a molecular complex between $HCO_3^-$ and $[HL]^+$, (2) the formation of $H_2O$ between $HCO_3^-$ Brønsted base and $[HL]^+$ Brønsted acid *via* a three-membered linear TS, and (3) the dissociation of the resultant products (L + $CO_2$ + $H_2O$). The **5-B-P** includes the EHHP of 55.5 kJ mol$^{-1}$ at 5-B-P-TS1 and the HER of 66.6 kJ mol$^{-1}$ at the reaction step of 5-B-P-IM1 → 5-B-P-TS1 → 5-B-P-IM2. The **5-B-N** involves the EHHP of 32.1 kJ mol$^{-1}$ at 5-B-N-TS1 and HER of 79.1 kJ mol$^{-1}$ at the reaction step of 5-B-N-IM1 → 5-B-N-TS1 → 5-B-N-IM2. The **5-B-Y** contains the EHHP of 36.6 kJ mol$^{-1}$ at 5-B-Y-TS1 and the HER of 47.7 kJ mol$^{-1}$ at the reaction step of 5-B-Y-IM1 → 5-B-Y-TS1 → 5-B-Y-IM2. It is indicated that these $[HL]^+$ kinetically increased as $[HPPh_3]^+$ < $[HPY]^+$ < $[HNEt_3]^+$ in neutralizing $HCO_3^-$.

Based on the above results, for the reaction I of LA + HCOOH → GVL + $H_2O$ + $CO_2$ catalyzed by $^6$[Ru(PPh$_3$)]$^{3+}$ with the additive $NEt_3$, the minimal energy reaction pathway (MERP) is made up of five reaction stages, *i.e.*, **1-F-N**, **2-F-S**, **3-F-K**, **4-F-C**, and **5-B-N**, namely, **GR-I**. The **GR-I** possesses the EHHP of 56.3 kJ mol$^{-1}$ at $^6$[3-F-K-TS2]$^{2+}$ and the HER of 94.3 kJ mol$^{-1}$ at the reaction step of $^6$[2-F-S-IM1]$^{2+}$ → $^6$[2-F-S-TS1]$^{2+}$ → $^6$[2-F-S-IM2]$^{2+}$ for the C–H bond cleavage of $HCOO^-$.

### 3.3 Reaction II: LA + HCOOH → OT + $H_2O$ + $CO_2$

The hydrodehydration of LA to OT with HCOOH as the hydrogen source comprises the aforementioned four reaction stages, *i.e.*, (i), (ii), (iv), and (v), and the following reaction stage (vi),

$$^6[RuH]^{2+} + LA \rightarrow {}^6[RuOH]^{2+} + OT \quad (vi)$$

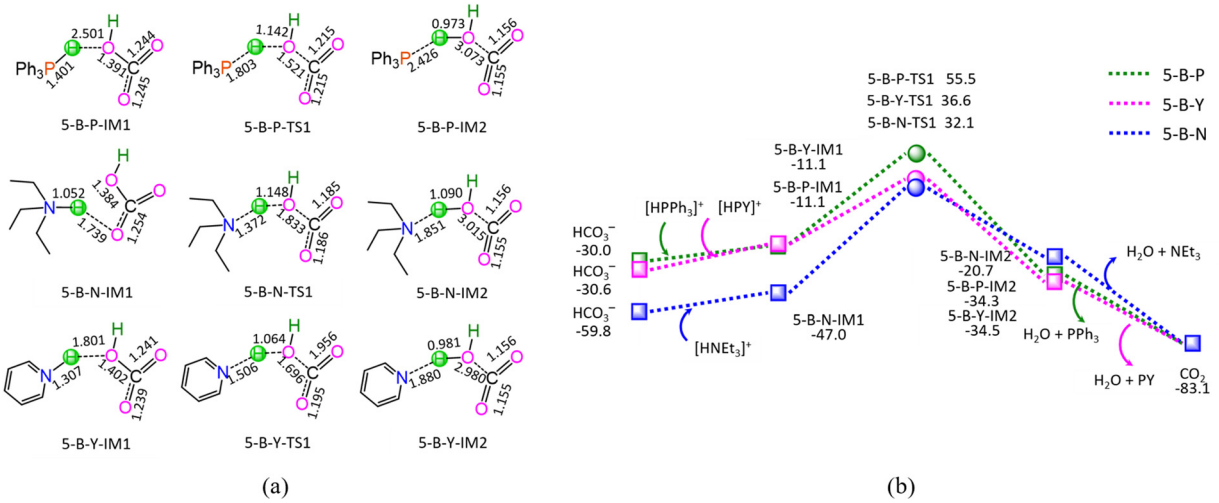


Fig. 5 The geometric structures (a) and the schematic energy diagrams (b) with the relative Gibbs free energy ($G_r$, kJ mol$^{-1}$) for the reaction stage (v) of $HCO_3^-$ + [HL]$^+$ → L + $CO_2$ + $H_2O$ (L = $PPh_3$, $NEt_3$, and PY). For clarity, hydrogen atoms on carbon are omitted. Bond lengths are presented in Å.

#### 3.3.1 Reaction stage (vi): $[RuH]^{2+}$ + LA → $[RuOH]^{2+}$ + OT.

Reaction stage (vi) is associated with the hydrogenation of LA with $^6[RuH]^{2+}$ hydride, producing OT and $^6[RuOH]^{2+}$ hydroxide. The geometric structures and potential energy diagrams for the reaction stage (vi) of $^6[RuH]^{2+}$ + LA → $^6[RuOH]^{2+}$ + OT are displayed in Fig. 6, through the initial interaction of Ru-site with the carboxyl carbonyl of LA, marked as **6-F-O**, respectively.

As shown in Fig. 6, the **6-F-O** includes four successive reaction steps, *i.e.*, (1) the formation of a molecular complex $^6[3\text{-F-C-IM4}]^{2+}$ through the initial interaction of Ru-site with the carboxyl carbonyl of LA, (2) a [2 + 2] addition at carboxyl carbonyl *via* four-membered cyclic $^6[6\text{-F-O-TS2}]^{2+}$ through a [1,3]-H shift with Ru–H bond cleavage, (3) the formation of OT with C1–OH bond cleavage through four-membered cyclic $^6[6\text{-F-O-TS3}]^{2+}$, and (4) the release of OT from $^6[6\text{-F-O-IM6}]^{2+}$, leaving $^6[RuOH]^{2+}$ hydroxide behind. The **6-F-O** involves the EHHP of 71.3 kJ mol$^{-1}$ at $^6[6\text{-F-O-TS2}]^{2+}$ for the Ru–H bond cleavage and HER of 72.0 kJ mol$^{-1}$ at the reaction step of $^6[6\text{-F-O-IM5}]^{2+}$ → $^6[6\text{-F-O-TS3}]^{2+}$ → $^6[6\text{-F-O-IM6}]^{2+}$ for the C1–OH bond cleavage.

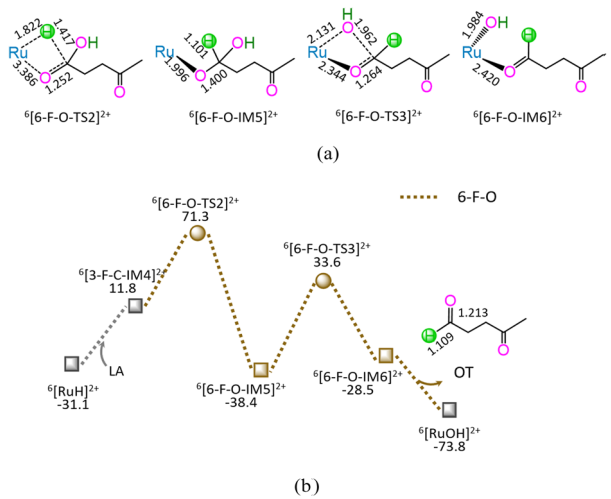


Fig. 6 The geometric structures (a) and the schematic energy diagrams (b) with the relative Gibbs free energy ($G_r$, kJ mol$^{-1}$) for the reaction stage (vi) of $^6[RuH]^{2+}$ + LA → $^6[RuOH]^{2+}$ + OT through the hydrogenation of carboxyl carbonyl. For clarity, hydrogen atoms on carbon are omitted. Bond lengths are presented in Å.

As mentioned earlier, for the reaction II of LA + HCOOH → OT + $H_2O$ + $CO_2$ catalyzed by $^6[Ru(PPh_3)]^{3+}$ with the additive $NEt_3$, the MERP is composed of five reaction stages, *i.e.*, **1-F-N**, **2-F-S**, **6-F-O**, **4-F-C**, and **5-B-N**, namely **GR-II**. The **GR-II** comprises the EHHP of 71.3 kJ mol$^{-1}$ at $^6[6\text{-F-O-TS2}]^{2+}$ for the Ru–H bond cleavage and the HER of 94.3 kJ mol$^{-1}$ at the reaction step of $^6[2\text{-F-S-IM1}]^{2+}$ → $^6[2\text{-F-S-TS1}]^{2+}$ → $^6[2\text{-F-S-IM2}]^{2+}$ for the C–H bond cleavage of $HCOO^-$.

### 3.4 Reaction III: LA + HCOOH → MFD + $CO_2$

The hydrogenation of LA to MFD with HCOOH as the hydrogen source includes the aforementioned two reaction stages, *i.e.*, (i) and (ii), and the following reaction stage (vii),

$$^6[RuH]^{2+} + LA + [HNEt_3]^+ + PPh_3 \rightarrow {}^6[Ru(PPh_3)]^{3+} + NEt_3 + MFD \quad \text{(vii)}$$

#### 3.4.1 Reaction stage (vii): $^6[RuH]^{2+}$ + LA + $[HNEt_3]^+$ + $PPh_3$ → $^6[Ru(PPh_3)]^{3+}$ + $NEt_3$ + MFD.

Reaction stage (vii) is concerned with the hydrogenation of LA with $^6[RuH]^{2+}$ hydride and $[HNEt_3]^+$, yielding MFD and regenerating the catalytically active species $^6[Ru(PPh_3)]^{3+}$. The geometric structures and potential energy diagrams for the reaction stage (vii) of $^6[RuH]^{2+}$ + LA + $[HNEt_3]^+$ + $PPh_3$ → $^6[Ru(PPh_3)]^{3+}$ + $NEt_3$ + MFD are shown in Fig. 7, through the initial interaction of Ru-site with the carboxyl carbonyl of LA, marked as **7-F-M**.

As depicted in Fig. 7, the **7-F-M** comprises seven successive reaction steps, *i.e.*, (1) the formation of a molecular complex $^6[3\text{-F-C-IM4}]^{2+}$, (2) a [2 + 2] addition at carboxyl carbonyl, (3) the

 

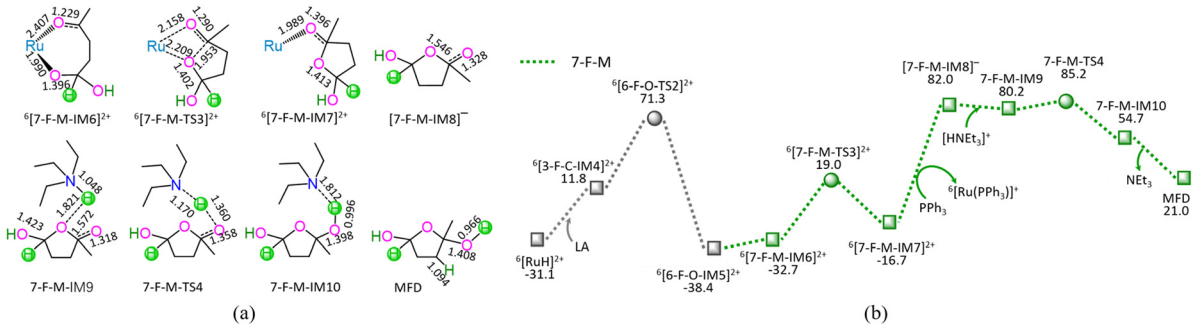


Fig. 7 The geometric structures (a) and the schematic energy diagrams (b) with the relative Gibbs free energy ($G_r$, kJ mol$^{-1}$) for the reaction stage (vii) of $^6[RuH]^{2+}$ + LA + $[HNEt_3]^+$ + $PPh_3$ → $^6[Ru(PPh_3)]^{3+}$ + $NEt_3$ + MFD through the hydrogenation of carboxyl carbonyl. For clarity, hydrogen atoms on carbon are omitted. Bond lengths are presented in Å.



molecular rearrangement between $^6[6\text{-F-O-IM5}]^{2+}$ and $^6[7\text{-F-M-IM6}]^{2+}$, (4) the ring-closure with C4–O bond formation *via* a seven-membered envelope $^6[7\text{-F-M-TS3}]^{2+}$, (5) the ligand–exchange between $^6[7\text{-F-M-IM7}]^{2+}$ and $PPh_3$, regenerating the catalytically active species $^6[Ru(PPh_3)]^{3+}$, (6) the formation of a molecular complex 7-F-M-IM9 between $[7\text{-F-M-IM8}]^-$ and $[HNEt_3]^+$, (7) the proton-exchange between $[7\text{-F-M-IM8}]^-$ and $[HNEt_3]^+$ *via* a three-membered linear 7-F-M-TS4, yielding a molecular complex 7-F-M-IM10, and (8) the dissociation of F-M-IM10 into free $NEt_3$ and MFD.

As mentioned earlier, for the reaction III of LA + HCOOH → MFD + $CO_2$ catalyzed by $^6[Ru(PPh_3)]^{3+}$ with the additive $NEt_3$, the MERP is composed of three reaction stages, *i.e.*, **1-F-N**, **2-F-S**, and **7-F-M**, namely, **GR-III**. The **GR-III** involves the EHHP of 85.2 kJ mol$^{-1}$ at $^6[F\text{-M-TS4}]^{2+}$ and HER of 98.7 kJ mol$^{-1}$ at the reaction step of $^6[7\text{-F-M-IM7}]^{2+}$ + $PPh_3$ → $[7\text{-F-M-IM8}]^-$ + $^6[Ru(PPh_3)]^{3+}$ for the regeneration of the catalytically active species $^6[Ru(PPh_3)]^{3+}$.

### 3.5 Reaction IV: LA + $H_2$ → GVL + $H_2O$

With $H_2$ as the hydrogen source, the hydrodehydration of LA to GVL includes the following sequential reaction stages (viii), (iii), (iv), and (v),

$$^6[Ru(PPh_3)]^{3+} + H_2 + L \rightarrow {}^6[RuH]^{2+} + [HL]^+ + PPh_3 \quad \text{(viii)}$$

**3.5.1 Reaction stage (viii): $^6[Ru(PPh_3)]^{3+}$ + $H_2$ + L → $^6[RuH]^{2+}$ + $[HL]^+$ + $PPh_3$.** Reaction stage (viii) is associated with the H–H bond cleavage catalyzed by $^6[Ru(PPh_3)]^{3+}$ with an organic base ligand (L = $PPh_3$, $NEt_3$, and PY), producing $[RuH]^{2+}$ hydride and $[HL]^+$ cation. The geometric structures and potential energy diagrams for the reaction stage (viii) of $^6[Ru(PPh_3)]^{3+}$ + $H_2$ + L → $^6[RuH]^{2+}$ + $[HL]^+$ + $PPh_3$ (L = $PPh_3$, $NEt_3$, and PY) are displayed in Fig. 8, marked as **8-H-P**, **8-H-N**, and **8-H-Y**, respectively.

As shown in Fig. 8, at the beginning, the ligand–exchange takes place between $^6[Ru(PPh_3)]^{3+}$ and $H_2$ molecule, forming a molecular complex $^6[Ru(H_2)]^{3+}$ and free $PPh_3$. From $^6[Ru(H_2)]^{3+}$, the H–H bond of $H_2$ undergoes homolysis, yielding a $^6[Ru(H)_2]^{3+}$ dihydride with the energy demand of 403.7 kJ mol$^{-1}$. Such a high requirement of 403.7 kJ mol$^{-1}$ makes H–H bond homolysis nearly impossible.

On the other hand, when the organic base ligand (L = $PPh_3$, $NEt_3$, and PY) participates in the H–H bond cleavage of $^6[Ru(H_2)]^{3+}$, the H–H bond of $H_2$ undergoes heterolysis *via* a

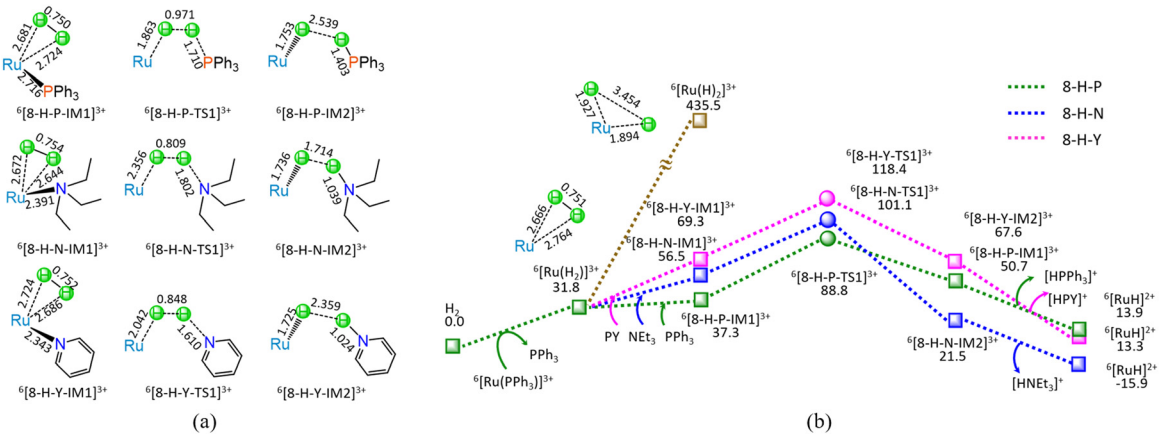


Fig. 8 The geometric structures (a) and the schematic energy diagrams (b) with the relative Gibbs free energy ($G_r$, kJ mol$^{-1}$) for the reaction stage (viii) of $^6[Ru(PPh_3)]^{3+}$ + $H_2$ + L → $^6[RuH]^{2+}$ + $[HL]^+$ + $PPh_3$ (L = $PPh_3$, $NEt_3$, and PY) and $^6[Ru(PPh_3)]^{3+}$ + $H_2$ → $^6[Ru(H)_2]^{3+}$. + $PPh_3$. For clarity, hydrogen atoms on carbon are omitted. Bond lengths are presented in Å.

four-membered U-type TS, producing a $^6[RuH]^{2+}$ hydride and $[HL]^+$ cation. The $\Delta G$ of reaction stage (viii) of $^6[Ru(PPh_3)]^{3+} + H_2 + L \rightarrow {}^6[RuH]^{2+} + [HL]^+ + PPh_3$ (L = $PPh_3$, $NEt_3$, and PY) is 13.9, −15.9, and 13.3 kJ mol$^{-1}$, respectively. It is indicated that the $NEt_3$ ligand is thermodynamically favourable, whereas both $PPh_3$ and PY are thermodynamically unfavourable. Kinetically, the **8-H-P**, **8-H-N**, and **8-H-Y** include the EHHP of 88.8, 101.1, and 118.4 kJ mol$^{-1}$, and the HER of 51.5, 44.6, and 49.1 kJ mol$^{-1}$, respectively. It is inferred that the promotive effect of the ligands kinetically increases as PY < $NEt_3$ < $PPh_3$ in the H–H bond heterolysis, because of their corresponding EHHPs of 118.4 > 101.1 > 88.8 kJ mol$^{-1}$. One can see that $NEt_3$ ligand should be preferable in the H–H bond heterolysis both thermodynamically and kinetically. Obviously, compared with the 403.7 kJ mol$^{-1}$ for the H–H bond homolysis, these organic base ligands (L = $PPh_3$, $NEt_3$, and PY) remarkably decrease the energy requirement for the H–H bond cleavage in $^6[Ru(H_2)]^{3+}$, because of their very lower EHHPs (88.8, 101.1, and 118.4 kJ mol$^{-1}$).

As mentioned earlier, for the reaction IV of LA + $H_2$ → GVL + $H_2O$ catalyzed by $^6[Ru(PPh_3)]^{3+}$ with the additive $NEt_3$, the MERP is made up of four reaction stages, *i.e.*, **8-H-N**, **3-F-K**, **4-F-C**, and **5-B-N**, namely, **GR-IV**. The **GR-IV** possesses the EHHP of 101.1 kJ mol$^{-1}$ at $^6[8\text{-H-N-TS1}]^{3+}$ for the H–H bond heterolysis, and HER of 79.1 kJ mol$^{-1}$ at the reaction step of 5-B-N-IM1 → 5-B-N-TS1 → 5-B-N-IM2 for the neutralization reaction between $HCO_3^-$ Brønsted base and $[HL]^+$ Brønsted acid. Furthermore, this result from **4-F-C** echoes that the additive $CO_2$ prominently promotes the Ru-OH bond cleavage of $^6[RuOH]^{2+}$, due to its Lewis acidity. Thereupon, this can explain why adding $CO_2$ can greatly improve the Ru-catalyzed hydrogenation with $H_2$ as the H source.[20]

### 3.6 Reaction V: LA + $H_2$ → OT + $H_2O$

For the reaction V of LA + $H_2$ → OT + $H_2O$ catalyzed by $^6[Ru(PPh_3)]^{3+}$ with the additive $NEt_3$, the MERP is composed of four sequential reaction stages, *i.e.*, **8-H-N**, **6-F-O**, **4-F-C**, and **5-B-N**, namely, **GR-V**. The **GR-V** comprises the EHHP of 101.1 kJ mol$^{-1}$ at $^6[8\text{-H-N-TS1}]^{3+}$ for the H–H bond heterolysis, and HER of 79.1 kJ mol$^{-1}$ at the reaction step of 5-B-N-IM1 → 5-B-N-TS1 → 5-B-N-IM2 for the neutralization reaction between $HCO_3^-$ Brønsted base and $[HL]^+$ Brønsted acid.

### 3.7 Reaction VI: LA + $H_2$ → MFD

For the reaction VI of LA + $H_2$ → MFD catalyzed by $^6[Ru(PPh_3)]^{3+}$ with the additive $NEt_3$, the MERP includes two reaction stages, *i.e.*, **8-H-N** and **7-F-M**, namely, **GR-VI**. The **GR-VI** involves the EHHP of 101.1 kJ mol$^{-1}$ at $^6[8\text{-H-N-TS1}]^{3+}$ for the H–H bond heterolysis, and HER of 98.7 kJ mol$^{-1}$ at the reaction step of $^6[7\text{-F-M-IM7}]^{2+} + PPh_3 \rightarrow [7\text{-F-M-IM8}]^- + {}^6[Ru(PPh_3)]^{3+}$ for the regeneration of the catalytically active species $^6[Ru(PPh_3)]^{3+}$.

### 3.8 Comparison of HCOOH with $H_2$ as the H-Source

As mentioned earlier, for the hydrogenation of LA with HCOOH or $H_2$ as the H source, their reaction pathways differ in the formed stage of $^6[RuH]^{2+}$ hydride, *i.e.*, reaction stages (**1-F-N** + **2-F-S**) with HCOOH as the H source, and reaction stage (**8-H-N**) with $H_2$ as the H source, whereas their reaction pathways after $^6[RuH]^{2+}$ hydride are identical. With HCOOH as the H source, the MERP for the formation of $^6[RuH]^{2+}$ hydride is associated with the reaction stages of both (i) (L = $NEt_3$) and (ii), namely, P-HCOOH. Besides, with $H_2$ as the H source, the MERP for the formation of $^6[RuH]^{2+}$ hydride is concerned with reaction stage (viii) (L = $NEt_3$), namely, P-$H_2$. Thereupon, we will kinetically compare the following reaction pathways, *i.e.*,

$$^6[Ru(PPh_3)]^{3+} + HCOOH + NEt_3 \rightarrow {}^6[RuH]^{2+} + [HNEt_3]^+ + PPh_3 + CO_2 \text{ (P-HCOOH)}$$

$$^6[Ru(PPh_3)]^{3+} + H_2 + NEt_3 \rightarrow {}^6[RuH]^{2+} + [HNEt_3]^+ + PPh_3 \text{ (P-}H_2\text{)}$$

In P-HCOOH, the rate-determining step is associated with $^6[2\text{-F-S-IM1}]^{2+} \rightarrow {}^6[2\text{-F-S-TS1}]^{2+} \rightarrow {}^6[2\text{-F-S-IM2}]^{2+}$ for the C–H bond cleavage and Ru–H bond formation. The corresponding rate constants $k_{\text{P-HCOOH}}$ can be adapted by the following expressions (in s$^{-1}$):

$$k_{\text{P-HCOOH}} = 2.80 \times 10^{13} \exp(-97\,523/RT) \quad (1)$$

Alternatively, in P–$H_2$, the rate-determining step is concerned with $^6[8\text{-H-N-IM1}]^{3+} \rightarrow {}^6[8\text{-H-N-TS1}]^{3+} \rightarrow {}^6[8\text{-H-N-IM2}]^{3+}$ for the H–H bond heterolysis and Ru–H bond formation. The corresponding rate constants can be described by the following expression (in s$^{-1}$):

$$k_{\text{P-H}_2} = 4.17 \times 10^{14} \exp(-56\,892/RT) \quad (2)$$

The rate constants of $k_{\text{P-H}_2}$ are computed to be about 5 orders of magnitude larger than those of $k_{\text{P-HCOOH}}$, over the temperature range 403–443 K. It is indicated that $H_2$ as the H source exhibits higher activity than HCOOH as the H source toward the formation of $^6[RuH]^{2+}$ hydride from $^6[Ru(PPh_3)]^{3+}$.

### 3.9 Origin of Selectively Generating GVL instead of OT and MFD

**3.9.1 Comparison of MFD with OT from the Hydrogenation of LA.** As mentioned earlier, after the formation of $^6[RuH]^{2+}$ hydride, if it initially interacts with the carboxyl carbonyl of LA, both OT and MFD can be produced, which are kinetically competitive with each other, namely, P–OT and P–MFD, respectively. As shown in Fig. 6 and 7, the reaction pathways of both P–OT and P–MFD are identical from the reaction stage of $^6[RuH]^{2+}$ + LA → $^6[6\text{-F-O-IM5}]^{2+}$. From $^6[6\text{-F-O-IM5}]^{2+}$, their selectivity-controlling steps are associated with $^6[6\text{-F-O-IM5}]^{2+} \rightarrow {}^6[6\text{-F-O-TS3}]^{2+} \rightarrow {}^6[6\text{-F-O-IM6}]^{2+}$ for the C1–OH bond cleavage in P-OT, and $^6[6\text{-F-O-IM5}]^{2+} \rightarrow {}^6[7\text{-F-M-TS3}]^{2+} \rightarrow {}^6[7\text{-F-M-IM7}]^{2+}$ for the C4–O1 bond formation of ring-closure in P-MFD. Then, the corresponding rate constants of $k_{\text{P-OT}}$ and $k_{\text{P-MFD}}$ can be fitted by the following expressions (in s$^{-1}$):

$$k_{\text{P-OT}} = 3.33 \times 10^{12} \exp(-68\,457/RT) \quad (3)$$

$$k_{\text{P-MFD}} = 5.00 \times 10^{10} \exp(-39\,136/RT) \quad (4)$$

 

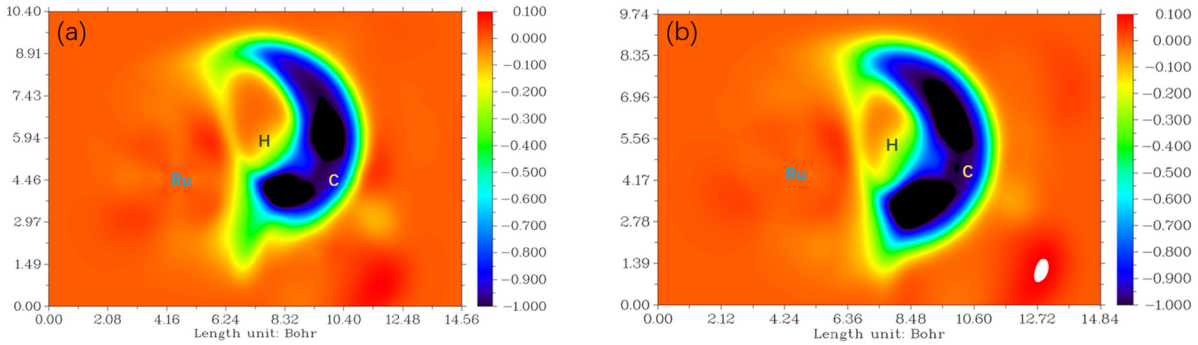


Fig. 9 The maps of differential electron localization function (DELF) for (a) $^{6}$[3-F-K-TS2]$^{2+}$ and (b) $^{6}$[6-F-O-TS2]$^{2+}$. The blue and especially dark blue regions represent the decrease in electron localization function.



The rate constants of $k_{\text{P-MFD}}$ are computed to be about 94–42 times larger than that of $k_{\text{P-OT}}$, over the temperature range 403–443 K. In view of $k_{\text{P-MFD}}$ and $k_{\text{P-OT}}$, their selectivities for P-MFD and P-OT are calculated to be 99.0–97.7% and 1.0∼2.3%, respectively. It is inferred that P-MFD is major, whereas P-OT is minor.

**3.9.2 Comparison of GVL with MFD from the Hydrogenation of LA.** As mentioned earlier, once $^{6}$[RuH]$^{2+}$ hydride is formed, the additions of both ketone carbonyl and carboxyl carbonyl of LA are competitive with each other, which correspond to the generation of GVL and MFD, respectively, namely, P-C═O and P-COOH. As shown in Fig. 3, 6, and 7, the selectivity-controlling steps are concerned with $^{6}$[RuH]$^{2+}$ + LA → $^{6}$[3-F-K-TS2]$^{2+}$ → $^{6}$[3-F-K-IM5]$^{2+}$ for the C4–H bond formation in P-C═O, and $^{6}$[RuH]$^{2+}$ + LA → $^{6}$[6-F-O-TS2]$^{2+}$ → $^{6}$[6-F-O-IM5]$^{2+}$ for the C1–H bond formation in P-COOH. The corresponding rate constants of $k_{\text{P-C=O}}$ and $k_{\text{P-COOH}}$ can be adapted by the following expressions (in $s^{-1}$ $mol^{-1}$ $dm^3$):

$$k_{\text{P-C=O}} = 4.12 \times 10^{6} \exp(-35\,530/RT) \quad (5)$$

$$k_{\text{P-COOH}} = 2.17 \times 10^{7} \exp(-56\,342/RT) \quad (6)$$

The rate constants of $k_{\text{P-C=O}}$ are calculated to be about 94–53 times larger than those of $k_{\text{P-COOH}}$, over the temperature range 403–443 K. Given $k_{\text{P-C=O}}$ and $k_{\text{P-COOH}}$, their selectivities for P-C═O and P-COOH are computed to be 99.0–98.2% and 1.0–1.8%, respectively. It is indicated that P-C═O is dominant, whereas P-COOH is secondary.

Here, the C–H bond formation is related to the C-site capturing the negatively charged $H^-$ from $^{6}$[RuH]$^{2+}$ hydride. In LA, the charge of C4 (+0.314) in the –C═O group is more positive than that of C1 (+0.003) in the –COOH group. Thereupon, the C4-site in the –C═O group more readily captures the negatively charged $H^-$ from $^{6}$[RuH]$^{2+}$ hydride than the C1-site in the –COOH group. One can expect that the C4–H bond in P-C═O is more readily formed than the C1–H bond in P-COOH.

To visualize the interaction of the forming C–H bond in $^{6}$[3-F-K-TS2]$^{2+}$ from P-C═O and $^{6}$[6-F-O-TS2]$^{2+}$ from P-COOH, the maps of differential electron localization function (DELF) are analyzed in Fig. 9. As depicted in Fig. 9, for the forming C–H bond region, the DELF region (blue and dark color) of $^{6}$[3-F-K-TS2]$^{2+}$ is narrower than that of $^{6}$[6-F-O-TS2]$^{2+}$. It is inferred that the C4–H bond formation in $^{6}$[3-F-K-TS2]$^{2+}$ from P-C═O more easily occurs than the C1–H bond formation in $^{6}$[6-F-O-TS2]$^{2+}$ from P-COOH.

## 4. Conclusion

The reaction mechanism for the hydrogenation of LA to GVL, OT and MFD catalyzed by Ru-containing species with HCOOH or $H_2$ as the hydrogen source in aqueous solution has been theoretically studied. The following conclusions can be drawn from the present results.

In aqueous solution with $PPh_3$ as an additive, a stable complex $^{6}$[Ru($PPh_3$)]$^{3+}$ can be formed after $RuCl_3{\cdot}3H_2O$ dissolves. Thereupon, $^{6}$[Ru($PPh_3$)]$^{3+}$ is preferred as the initial catalytically active species.

Kinetically, the hydrodehydration of LA to GVL is predominant through the hydrogenation of ketone carbonyl, with OT and MFD as side-products through the hydrogenation of carboxyl carbonyl. This stems from the more positive charge of C4 (+0.314) in the –C═O group than that of C1 (+0.003) in the –COOH group in LA. Herein, the C4-site in the –C═O group more easily sieves the negatively charged $H^-$ from [RuH]$^{2+}$ hydride than the C1-site in the –COOH group.

With HCOOH as the H source, initially, the OBL, *e.g.*, triethylamine, pyridine, or triphenylphosphine, is responsible for grabbing the proton $H^+$ from HCOOH, resulting in both $HCOO^-$ and $[HL]^+$. Next, the $Ru^{3+}$-site undertakes to capture the $H^-$ from $HCOO^-$, generating both [RuH]$^{2+}$ hydride and $CO_2$. Besides, with $H_2$ as the H source, the OBL promotes the heterolytic H–H bond with the aid of $Ru^{3+}$-active species, yielding both [RuH]$^{2+}$ hydride and $[HL]^+$. Toward the formation of [RuH]$^{2+}$ hydride, $H_2$ as the H source displays higher activity than HCOOH as the H source in the presence of an OBL.

And then, the $H^-$ in [RuH]$^{2+}$ hydride transfers to the unsaturated C-site of ketone carbonyl in LA. Afterwards, the $Ru^{3+}$-active species is responsible for the C–OH bond cleavage in 4-hydroxyvaleric acid, producing both [RuOH]$^{2+}$ hydroxide and GVL. After that, $CO_2$ promotes the Ru–OH bond cleavage in [RuOH]$^{2+}$ hydroxide, forming $HCO_3^-$ and regenerating the $Ru^{3+}$-active species, because of its Lewis-acidity. Subsequently,

neutralization reaction occurs between the resultant $HCO_3^-$ and $[HL]^+$, yielding $H_2O$, $CO_2$, and OBL.

## Author contributions

The manuscript was written through the contributions of all the authors. H.-Y. Min is responsible for the data curation, investigation formal analysis and writing – original draft, J.-S. Xiong, and T.-H. Liu are responsible for formal analysis, S. Fu for data curation, H.-Q. Yang is responsible for the conceptualization, methodology, resources, project administration, formal analysis, supervision and writing – review & editing, and C.-W. Hu is responsible for the supervision and resources. All authors have given approval to the final version of the manuscript.

## Conflicts of interest

There are no conflicts to declare.

## Acknowledgements

The authors are grateful for financial support by the National Natural Science Foundation of China (No: 22073064) and the 111 Project (No: B17030).

## Notes and references

1 B. Y. Karlinskii and V. P. Ananikov, *Chem. Soc. Rev.*, 2023, **52**, 836–862.
2 M. Sajid, U. Farooq, G. Bary, M. M. Azim and X. B. Zhao, *Green Chem.*, 2021, **23**, 9198–9238.
3 Y. W. Shao, K. Sun, Q. Y. Li, Q. H. Liu, S. Zhang, Q. Liu, G. Z. Hu and X. Hu, *Green Chem.*, 2019, **21**, 4499–4511.
4 T. Raj, K. Chandrasekhar, R. Banu, J. J. Yoon, G. Kumar and S. H. Kim, *Fuel*, 2021, **303**, 121333.
5 C. Q. Deng, J. Liu, J. H. Luo, L. J. Gan, J. Deng and Y. Fu, *Angew. Chem., Int. Ed.*, 2022, **61**, e202115983.
6 J. S. Yang, R. D. Shi and G. B. Zhou, *Chem. Eng. J.*, 2023, **475**, 146297.
7 M. Kondeboina, S. S. Enumula, K. S. Reddy, P. Challa, D. R. Burri and S. R. R. Kamaraju, *Fuel*, 2021, **285**, 119094.
8 J. Bai, C. W. Cheng, Y. Liu, C. G. Wang, Y. H. Liao, L. G. Chen and L. L. Ma, *Mol. Catal.*, 2021, **516**, 112000.
9 E. Soszka, O. Sneka-Płatek, E. Skiba, W. Maniukiewicz, A. Pawlaczyk, J. Rogowski, M. Szynkowska-Jóźwik and A. M. Ruppert, *Fuel*, 2022, **319**, 123646.
10 A. M. Ruppert, M. Jędrzejczyk, O. Sneka-Płatek, N. Keller, A. S. Dumon, C. Michel, P. Sautet and J. Grams, *Green Chem.*, 2016, **18**, 2014–2028.
11 J. Molleti, M. S. Tiwari and G. D. Yadav, *Chem. Eng. J.*, 2018, **334**, 2488–2499.
12 Z. Z. Wei, X. F. Li, J. Deng, H. R. Li and Y. Wang, *Mol. Catal.*, 2018, **448**, 100–107.
13 Y. W. Lu, Y. X. Wang, Y. H. Wang, Q. Cao, X. G. Xie and W. H. Fang, *Mol. Catal.*, 2020, **493**, 111097.
14 Z. Z. Liu, X. Y. Gao and G. Y. Song, *Chem. Eng. J.*, 2023, **470**, 143869.
15 N. Siddiqui, C. Pendem, R. Goyal, R. Khatun, T. S. Khan, C. Samanta, K. Chiang, K. Shah, M. A. Haider and R. Bal, *Fuel*, 2022, **323**, 124272.
16 T. Y. Deng, L. Yan, X. L. Li and Y. Fu, *ChemSusChem*, 2019, **12**, 3837–3848.
17 J. J. Lu, Y. Wei, K. Y. Lu, C. M. Wu, X. Y. Nong, J. F. Li, C. L. Liu and W. S. Dong, *Mol. Catal.*, 2022, **527**, 112409.
18 C. C. Li, C. H. Hsieh and Y. C. Lin, *Mol. Catal.*, 2022, **523**, 111720.
19 Q. Xu, X. L. Li, T. Pan, C. G. Yu, J. Deng, Q. X. Guo and Y. Fu, *Green Chem.*, 2016, **18**, 1287–1294.
20 L. Deng, J. Li, D. M. Lai, Y. Fu and Q. X. Guo, *Angew. Chem., Int. Ed.*, 2009, **48**, 6529–6532.
21 J. M. Tukacs, B. Fridrich, G. Dibó, E. Székely and L. T. Mika, *Green Chem.*, 2015, **17**, 5189–5195.
22 C. Moustani, E. Anagnostopoulou, K. Krommyda, C. Panopoulou, K. G. Koukoulakis, E. B. Bakeas and G. Papadogianakis, *Appl. Catal., B*, 2018, **238**, 82–92.
23 C. A. M. R. van Slagmaat and S. M. A. De Wildeman, *Eur. J. Inorg. Chem.*, 2018, 694–702.
24 V. S. Shende, A. B. Raut, P. Raghav, A. A. Kelkar and B. M. Bhanage, *ACS Omega*, 2019, **4**, 19491–19498.
25 W. Li, J. H. Xie, H. Lin and Q. L. Zhou, *Green Chem.*, 2012, **14**, 2388–2930.
26 J. Deng, Y. Wang, T. Pan, Q. Xu, Q. X. Guo and Y. Fu, *ChemSusChem*, 2013, **6**, 1163–1167.
27 S. D. Wang, V. Dorcet, T. Roisnel, C. Bruneau and C. Fischmeister, *Organometallics*, 2017, **36**, 708–713.
28 C. Ortiz-Cervantes, M. Flores-Alamo and J. J. García, *ACS Catal.*, 2015, **5**, 1424–1431.
29 B. Zada, R. Zhu, B. Wang, J. Liu, J. Deng and Y. Fu, *Green Chem.*, 2020, **22**, 3427–3432.
30 W. R. H. Wright and R. Palkovits, *ChemSusChem*, 2012, **5**, 1657–1667.
31 M. J. Frisch, G. W. Trucks, H. B. Schlegel, G. E. Scuseria, M. A. Robb, J. R. Cheeseman, G. Scalmani, V. Barone, B. Mennucci and G. A. E. A. Petersson, *Revision C.01*, Gaussian Inc., Wallingford, CT, 2010.
32 M. Cossi, G. Scalmani, N. Rega and V. Barone, *J. Chem. Phys.*, 2002, **117**, 43–54.
33 A. V. Marenich, C. J. Cramer and D. G. Truhlar, *J. Phys. Chem. B*, 2009, **113**, 6378–6396.
34 Y. Zhao and D. G. Truhlar, *Theor. Chem. Acc.*, 2008, **120**, 215–241.
35 F. Weigend and R. Ahlrichs, *Phys. Chem. Chem. Phys.*, 2005, **7**, 3297.
36 A. D. McLean and G. S. Chandler, *J. Chem. Phys.*, 1980, **72**, 5639–5648.
37 R. Krishnan, J. S. Binkley, R. Seeger and J. A. Pople, *J. Chem. Phys.*, 1980, **72**, 650–654.
38 P. C. Hariharan and J. A. Pople, *Theor. Chim. Acta*, 1973, **28**, 213–222.

 

39 C. Gonzalez and H. B. Schlegel, *J. Chem. Phys.*, 1989, **90**, 2154–2161.
40 C. Gonzalez and H. B. Schlegel, *J. Chem. Phys.*, 1990, **94**, 5523–5527.
41 A. E. Reed, R. B. Weinstock and F. Weinhold, *J. Chem. Phys.*, 1985, **83**, 735–746.
42 A. E. Reed, L. A. Curtiss and F. Weinhold, *Chem. Rev.*, 1988, **88**, 899–926.
43 T. Lu and F. W. Chen, *J. Comput. Chem.*, 2012, **33**, 580–592.
44 T. Lu and F. W. Chen, *J. Mol. Graphics Modell.*, 2012, **38**, 314–323.
45 L. K. Ren, L. F. Zhu, T. Qi, J. Q. Tang, H. Q. Yang and C. W. Hu, *ACS Catal.*, 2017, **7**, 2199–2212.
46 B. Xiang, Y. Wang, T. Qi, H. Q. Yang and C. W. Hu, *J. Catal.*, 2017, **352**, 586–598.